Metal–Matrix Composites from High-Pressure Torsion with Functionalized Material Behavior

Valeria Lemkova, Juraj Todt, Christian Motz, and Florian Schaefer*

In composites, outstanding properties of two materials can be combined. In particular, metal–matrix composites (MMCs) can combine the properties of a high-strength ductile metallic matrix with special properties of embedded ceramic particles. This hybrid can be used to create a functional material. However, during consolidation, the thermal load of most common MMC-processing routes is an obstacle for such functionalization, because the unique properties of the ceramic phases most likely degrade. Mechanical alloying, in this case, by high-pressure torsion (HPT), can overcome this challenge. Herein, the attempt to obtain smart materials through HPT processing is aimed. For that purpose, Cu-MMCs are produced from mixed powders with ZrO_2 and $BaTiO_3$ (BTO) with the challenge to incorporate their functional phase. BTO can provide a sensing ability for internal stress and ZrO_2 can provide a fatigue lifetime by a retarded crack growth. The amount of the stabilized phase is evaluated by X-ray diffraction. Cu–BTO–MMCs exhibit a local piezoelectric effect when strained, shown by in situ scanning Kelvin probe force microscopy. Cu–ZrO_2–MMCs feature a retarded fatigue crack initiation and an earlier crack closure during fatigue crack growth due to the volume expansion once ZrO_2 transforms.

1. Introduction

Metal–matrix composites (MMCs), as the name implies, consist of a continuous metallic matrix and disseminated embedded ceramic or organic reinforcements. Particle reinforcements of ceramic nature offer the unique opportunity to combine the ductile and tough nature of metals with ceramic traits, like thermal stability or wear resistance. Because of their outstanding properties, MMCs are already implemented, for example, in aerospace and automotive and electronic components.[1,2] Another improvement of such MMCs is to provide the ceramic particles or the metallic matrix with an additional function. For instance, using graphene as an additive to a metallic matrix, a self-lubrication can be achieved.[2] Furthermore, abilities like enhanced damping or grain boundary pinning could also be gained.[3] In the context of self-healing, a notable functionalization of MMCs is the use of shape memory alloy wires incorporated into a metallic matrix, that contract through straining of the fractured matrix. This contraction shrinks the size of the component, but supports overall structural integrity.[2,4,5]

For the synthesis of MMCs, two main approaches exist, a bottom–up and a top–down. In the former case, particles configure during synthesis by a chemical reaction or by precipitation. In the top–down case, both components are already in their near-final state, but need to reach final configuration by synthesis.[6] Casting is a typical top–down route example but owns further challenges. For instance, the thermal load might degrade the properties of the embedded particles. Additionally, agglomeration of particles or porosity and other inhomogeneity are still a problem.[2,5,7]

High-pressure torsion (HPT), a method of severe plastic deformation, allows not only to achieve an ultrafine-grained metallic matrix but also mechanical alloying without thermal load. Disclike samples are produced by pressing and rotating two anvils against each other. The input material (powder or bulk material) can experience pressure up to 40 GPa, depending on the capabilities of the HPT system.[8] Additionally, it has been demonstrated that high-pressure phases can be effectively stabilized in MMCs.[9] For high-pressure phases of oxide ceramics residual stresses originating from the large plastic deformation during HPT are the main cause for stabilization.[1,10] MMCs consisting of Cu and tetragonal $BaTiO_3$ (t-BTO) were already synthesized under moderate pressure and these exhibited an improved damping ability against mechanical vibrations in comparison to pure Cu.[11]

With the aim to achieve smart intelligent material behavior by the means of HPT processing, this work focuses on two possible abilities. First, with the incorporation of t-BTO, the ambient pressure phase with piezoelectric properties, it could be possible to detect an electric polarization as a response to strain. Such (Cu)–BTO–MMCs could react to internal and external stresses,

V. Lemkova, C. Motz, F. Schaefer
Materials Science and Methods
Saarland University
Campus D2 3, 66123 Saarbruecken, Germany
E-mail: f.schaefer@matsci.uni-sb.de

J. Todt
Materials Physics
Montanuniversitaet Leoben
Jahnstr. 12, 8700 Leoben, Austria

The ORCID identification number(s) for the author(s) of this article can be found under https://doi.org/10.1002/adem.202201565.

and therefore elucidate on material damage as a self-sensing material. Second, with the help of zirconia (ZrO_2), the prevention of early failure by impeding crack initiation and inhibiting further crack growth can be achieved. This is due to the transformation of the intermediate temperature tetragonal phase to its ambient pressure and ambient temperature monoclinic phase, and the associated large volume expansion of 3–4%. Cu was chosen due to its low health risk and easy handling in bulk and powder forms. In addition to its ductile nature, strongly pronounced thermal/electrical conductivity and bactericidal features,[12] Cu is an attractive material also due to its well-known properties during HPT. In principle, the matrix material is replaceable. Furthermore, the dispersed ceramic particles can also avoid grain coarsening during the HPT process and thus diminish the achieved grain size and strengthen the Cu matrix. Additionally, the particles might further stabilize the grain boundaries and hence improve thermal stability.[3,6]

The following questions shall be clarified with this work: 1) Is it possible to implement ZrO_2 and BTO particles into MMCs via HPT? 2) Do the implemented ceramics with their characteristic properties provide the desired functionalization?

This manuscript is organized as follows: an introduction on the ceramic particles is given in Section 2. In Section 3, the experimental methods are provided. Section 4 contains the synthesis methods and Section 5 contains a short microstructural analysis and investigation of thermal stability. In Section 6, the results for the BTO-based functionalization of Cu are shown whereas Section 7 focuses on zirconia embedded in Cu. The conclusion is provided in Section 8.

2. Materials

2.1. Ceramic Embedments

2.1.1. BTO

$BaTiO_3$ is a perovskite with ferroelectric property, which describes the feature of a switchable electric polarization by an external electric field or mechanical stress. At ambient conditions, BTO has a tetragonal crystal structure with piezoelectric properties. This feature is the key for the purpose of functionalization, as the piezoelectric effect scales with applied strain. This effect can be measured using either a Sawyer–Tower circuit or scanning Kelvin probe force microscopy (SKPFM). In the former, the sample would be used as one half of a capacitor.[13] The latter is able to image any changes in the electric field and the capacitance between sample and an atomic force microscopy tip.[14,15] This phenomenon applies to ABO_3 perovskites due to their crystallographic structure. For BTO, Ti occupies the body-centered position, as in a perfect cubic perovskite structure. A tetragonal phase transition with a low c to a ratio of just 1.011 is induced by a displacement of the Ti atom; a stretching of the lattice.[16,17] The displacement is either along soft modes by 11.7° or by hard polarization along the (111) axis.[17,18]

Hydrostatic pressure, similar to temperature as a thermodynamic condition, causes a phase transition between the tetragonal and the cubic phase. During the production of these MMCs, the high pressure of the HPT could cause a phase transformation

of the BTO, since at either higher pressure (≥ 2 GPa) or at higher temperature (≥ 120 °C) a cubic phase is stable, resulting in paraelectric properties.[19,20] But nonetheless, phase transitions due to a temperature or a pressure change are considered distinctly different. The BTO phase transition at ambient pressures with increasing temperatures is considered to be a tetragonal-cubic phase transition of first order, whilst the pressure-induced phase transition at room temperature is considered to be of second order, also called a continuous phase transition. The shift from first to second order is rather gradual than abrupt. For the pressure-induced phase transition, the cubic phase can be stabilized starting from 1.8 to 3 GPa at ambient temperature, depending on the authors of ref. [17].

However, the transition is also influenced by the grain size. The transition temperature and piezo-coefficient decrease with decreasing particle and/or grain size.[21–23] For a grain size below 100 nm, the macroscopic crystallographic structure of BTO was found to be cubic.[24] X-Ray absorption fine-structure analysis and Raman spectroscopy revealed that the Ti atom is still displaced from the center position if the grain size is below 100 nm.[25] This structure is called quasi-cubic. Furthermore, with increasing pressure, the symmetry of the unit cell increases.[17]

Devonshire tried to explain the grain size effect from the point of view of surface phenomena, leading to a structural interpretation.[26,27] There, the structure of BTO encompasses a cubic shell, a tetragonal BTO core and a gradient lattice strain layer in between. This layer exhibits a gradually changing lattice parameter, while the thickness of the cubic shell is independent of the size of the core–shell particle (8 nm shell thickness). This means the smaller the particles the higher the cubic phase ratio at room temperature (disregarding the transition layer). According to this model, particles with the size of ≈20 nm should be completely cubic.[28,29]

Venkateswaran et al.[30] proposed that some disorder is always present in the cubic phase at moderate pressure and at ambient temperature. This disorder in polycrystalline samples is not only due to a slight off-center position of Ti in the unit cell, caused by the order/disorder model ranging from ferroelectric to paraelectric,[16] but can also result from grain boundaries, inter-grain stress from MMC matrix pressure and from a shift of atomic positions under high pressure.

Up to now, BTO has scarcely been applied for MMCs in general[11] and especially for MMCs prepared by HPT. Since particles with at least 100 nm size partially undergo the cubic transition, it is likely that the phase fraction of cubic BTO increases with increasing applied HPT revolutions, because this reduces the grain size, before a plateau is reached.[28,29,31] The difference between grain size and particle size also has to be considered

Table 1. Applied metals and ceramics and their elastic moduli[58–60] and powder sizes. (ZrO_2 grain size analyzed by SEM and LuMisizer).

Metal	Modulus [GPa]	Max. size [µm]	Ceramic	Modulus [GPa]	Mesh/particle size [µm]
Cu	120	10–25	BTO-a	105	<2
			BTO-b	105	<45
Cu	120	45	ZrO_2	220	0.003–20

2201565 (2 of 12)

in this context. Therefore, an ongoing phase transformation during the HPT process is expected. Furthermore, the mechanical contrast between the matrix material and BTO during HPT revolutions, which in this case is moderate (see **Table 1**), can lead to residual stresses that stabilize the cubic BTO. However, considering the yield stress of Cu after HPT production, these internal stresses in the vicinity of the particles are expected to be well below 1 GPa and are influenced by aging.

If SKPFM is used as proof for the functionalization for the manufactured BTO–MMCs, then the signal is expected to differ between the cubic and tetragonal phase when scanning over the ceramic embedment. This difference occurs either due to a missing polarization as a consequence of paraelectricity of the cubic phase[32] or due to a difference in the work function between t- and c-BTO. The electric field directly reacts on an evolving piezoelectric effect.

2.1.2. Zirconia

ZrO_2 has an intermediate temperature tetragonal phase that can be stabilized down to room temperature. Due to its anisotropic increase of volume of about 3% induced by a martensitic phase transformation from the intermediate temperature tetragonal to the monoclinic phase,[33,34] that is stable at room temperature for pure ZrO_2. ZrO_2 has already been widely studied regarding MMCs and self-healing traits.[6,35–37] The atoms coordinate diffusionlessly to a slightly different lattice with a different orientation rather than switching atomic positions.

The mechanism of crack closure by this martensitic transformation in ZrO_2 has been researched in particular by Evans and Heuer[38] and their assumptions are still state of the art. t-ZrO_2 undergoes this transformation, associated with the desired volume increase at standard ambient conditions when tensile stress is applied.[39]

To utilize this self-healing mechanism, t-ZrO_2 has to be incorporated and stabilized, also during HPT or even supported by HPT. In the expected pressure range via HPT (up to 7.7 GPa), by considering the phase diagram of ZrO_2, the resulting phase would however be the orthorhombic-I phase (above 3–4 GPa). The desired tetragonal phase is stabilized by high temperatures above 500 °C.[39] Additional mechanisms contribution to stabilization of non-ambient ZrO_2 phases are 1) compressive constraint by a surrounding matrix, for example, in MMCs,[40] 2) doping with yttria,[10,39] and 3) a small grain size, promoting a size effect.[38–40]

The seems feasible, as described by Abu et al.[41] for ball milling, a synthesis method with similar deformation to HPT. They reported that the addition of about 5–10% of ZrO_2 to Cu resulted in a harder matrix and reduced grain size for both of the species.

3. Experimental Section

3.1. Microstructural and Thermal-Analysis

As part of the study of thermal stability and microsturcture, the following procedures were used: electron backscatter diffraction (EBSD) imaging (EBSD, Nordlys nano detector with the software Aztec, Oxford Instruments), scanning electron microscope and transmission Kikuchi diffraction (TKD) (Zeiss Sigma VP field-emission). The preparation for TKD was done via classical transmission electron microscope preparation. This included mechanical grinding and polished to about 10 μm and finishing by Ar-ion polishing using Gatan PIPS (Precision Ion Polishing System). Target preparation with focused-ion beam was not used, because it was observed that the grain size increased due to the energy input. The electrochemical route was tried, but due to the ceramic particles behaving differently from the pure copper matrix, the edges of the thinned holes became too frayed and unstable. To determine thermal stability, isochronal heat treatments were executed in ambient air between 100 and 500 °C, alongside hardness measurements at every step.

3.2. Phase Analysis

To analyze the amount of obtained high-pressure phase, X-Ray diffraction (XRD) analysis (Rigaku SmartLab 5 cycle equipped with Cu-K_α radiation, primary parabolic multi-layer mirror and secondary graphite monochromator) was employed. Because of time restrictions diffractograms were taken in restricted angular ranges, for samples with BTO between 20°–35° and 53°–70° and for samples with ZrO_2 between 20°–38° and 53°–68°. The chosen step size was 0.05°, with a counting time of 15 s step^{-1}.[42,43] Rietveld refinement was employed to obtain information about quantitative phase fractions, especially for BTO samples, also showing the validity of the refinement due to different matching results with cubic BTO and without.

3.3. SKPFM

To measure the functionalization of MMCs with BTO, SKPFM analysis was performed using a Bruker Dimension Icon/ Fastscan instrument. The bias voltage was set to 1 V and the frequency modulation (FM) mode was selected. An adapted Kammrath & Weiss bending module was used to bend the sample to introduce mechanical stress and to induce a phase transformation of BTO. For this, the HPT samples were drilled and screwed down to a brass sample holder (see **Figure 1**). After bending, the sample was measured again under the same conditions and at the same position with the SKPFM setup. The resulting images were analyzed using the software Gwyddion.
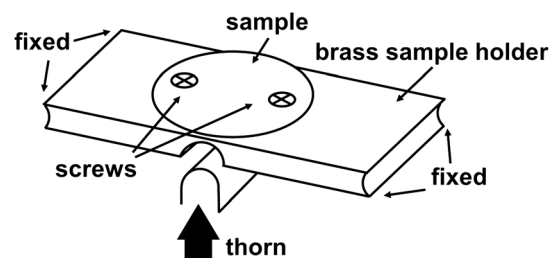

Figure 1. Parts of the bending module with the a specimen fixed with screws.

**ADVANCED
SCIENCE NEWS**

www.advancedsciencenews.com

**ADVANCED
ENGINEERING
MATERIALS**

www.aem-journal.com

Table 2. Geometric parameters ($B =$ thickness, $a =$ crack length, $W =$ length to the point of force application) of the 8.2 GPa large HPT samples.

Sample	B [mm]	a [mm]	W [mm]
Cu Ref	0.400	0.182390	0.85
Cu bulk	0.404	0.187192	0.85
Cu ZrO$_2$	0.396	0.2027155	0.85
Cu ZrO$_2$	0.404	0.209164	0.85

Table 3. Tested ΔK for the two reference samples and two samples with ZrO$_2$. ▨ indicates ΔK underneath the intrinsic fatigue propagation threshold $\Delta K_{th,eff}$, ▨ indicates $\Delta K_{th,eff} < \Delta K < \Delta K_{th}$, and ▨ the fatigue crack propagation ΔK_{th}.

ΔK	1.6	1.7	1.8	1.9	2.0	2.1	2.2	2.5
Cu Ref 8.2 GPa	🟩			🟥			🟥	🟥
Cu ZrO$_2$ 8.2 GPa	⬜	⬜	⬜	🟩	🟩	🟩	🟥	

3.4. da/dN-Curve Tests with Crack Closure

Following DIN EN ISO 12 737 and ASTM E1820-11, compact tension (ct) samples with adjusted sizes (see **Table 2**) were prepared from the large HPT specimens (see **Table 3**). The testing itself did not follow the standards precisely, to exclude artifacts from plasticity-induced crack closure. All other conditions remained as described in the standard procedure. It was expected that retarded crack growth (with decreased intrinsic fatigue crack propagation threshold [$\Delta K_{th,eff}$]) according to ref. [44] was related to an increase in roughness-induced crack closure.

Razor blade polishing of the notches was cut in the short crack order.[45] To avoid compressive residual stress and plasticity effects, a short crack was generated through compression precracking. The same hydraulic press model as for HPT was used for this purpose. The specimens were placed between two flat metallic plungers and compressed for 20 000 cycles, so that there was always contact between the specimen and the structure (no tensile load). Similar to the subsequent tests, the force to produce a short crack was determined using the aforementioned standards. After this, the fatigue testing was performed, with gradually increasing load (with an amplitude at a constant stress ratio of $R = 0.1$), also called *cyclic R-curve*, to determine the intrinsic $\Delta K_{th,eff}$.

The fixture for current pick-up to measure crack extension was 3D printed and the contact pins were attached with adhesive. To avoid the Seebeck effect, an additional reverse polarity device was attached to the used nano-voltmeter (Keithley 2182 A), to change the current direction every few seconds.

After reaching the fatigue crack propagation threshold, the crack led to fracturing. Since we stopped the cycling at the $\Delta K_{th_{test}}$ level, stress-sensitivity factor (K_{IC}) was also determined according to ASTM E399. To measure the crack length during cycling, the direct current potential drop method (DCPD) was employed. The ct sample was provided with a constant current
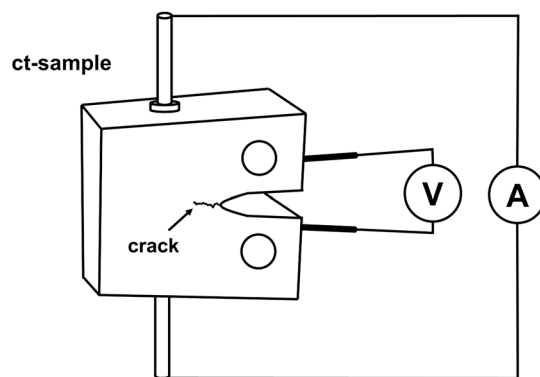

Figure 2. Compact tension sample with the bonding for DCPD method.

(2 Å) from the parallel sides of the notch (see **Figure 2**). By extension of the crack, the electrical distance between the two measuring points increased and so did the resistance.

Before the experiment, the sample was brought into a statically heated state (working temperature), so that no unexpected temperature variations affected the electrical resistance and thus the electrical signal. Knowing the dimensions of the samples, the crack length a was then calculated by the Johnson formula using the measured voltage.[46,47] Thereafter, the crack velocity ($\partial a / \partial N$) was shown against N (cycles) for the individual samples and against the stress-intensity factor ΔK. Since the fracture surfaces were accessible, the final crack length before fracture could be measured via optical microscope. The measured values between repeated samples were sufficiently similar and therefore not adjusted additionally. As the ceramic content of the MMCs was ≤10 wt%, its effect on the overall elastic modulus, and therefore on ΔK_{th}, could be neglected. This is important, as a drop in the fatigue crack propagation threshold, if comparing samples with and without ZrO$_2$, would imply a lifetime decrease due to faster crack growth.

4. Synthesis

With HPT, grain refinement down to the nanocrystalline regime can be achieved (e.g., in Cu). The low thermal stability of this class of nanostructured materials is a challenge, since the large number of grain boundaries favors premature grain growth.[48] If a powder is used instead of a bulk precursor material, the hardness and thermal stability increase in most cases. Grain boundary pin due to the increased amount of oxides introduced with the powder and therefore promotes further grain refinement and microstructural stability.[49] For further investigation, HPT–Cu from the powder route, consolidated at room temperature, acts as a reference material for all tested MMCs.

For the purposes of synthesis via HPT, the powders according to Table 1 were mixed. A simple scale was used for this purpose, the mixing was done with a spatula. The powders were filled into a Cu ring attached to the lower anvil (made from S390 tool steel) as seen in **Figure 3**a. After positioning, the powder-loaded lower anvil and the opposing upper anvil (also S390) inside the HPT system (Schenck Fert. Nr. PCW 00 181 975), a green body was
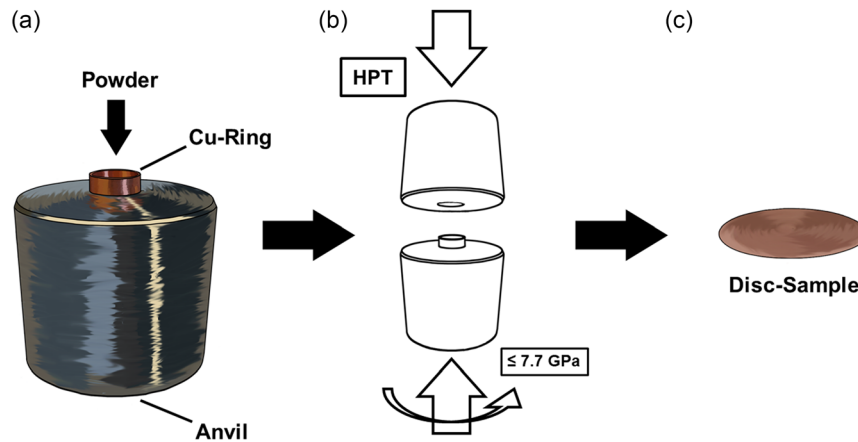
ADVANCED
SCIENCE NEWS
www.advancedsciencenews.com

ADVANCED
ENGINEERING
MATERIALS
www.aem-journal.com

Figure 3. Flowchart for the sample preparation: a) the S390 lower anvil with attached Cu ring to contain the powder mixture, b) the high-pressure torsion process, and c) the resulting disclike sample.

pressed inside of the respective cavities. The applied pressure is assumed to be hydrostatic. During the entire sample manufacturing process, the rate of counterrotation was kept constant at 0.7 rpm. The resulting disc-shaped samples (see Figure 3c) had diameters of 8 mm ($2r$) with a sample thickness (t) of $\approx$0.6 mm.

Since the v. Mises equivalent strain ε_{eq} follows Equation (1)

$$\varepsilon_{eq} = \frac{2 \times \pi \times n \times r}{t\sqrt{3}} \tag{1}$$

with number of turns n, measuring hardness at a constant radius position from the center of the disks with a constant thickness t guarantees a comparable ε_{eq} just depending on n.

To determine the phase fraction, a mass percentage of the ceramic particles of 10 wt% was used, to allow a phase analysis via XRD (see **Table 4**).

In reference to Table 4, the minimal pressure for BTO was chosen to be moderately above the presumed phase-transition pressure to analyze phase fraction growth from lowest to highest and to see possible disordered cubic phase effects in the samples.[30] To further determine the leverage of strain on the phase transition, the rotation number varied between 1, 5, 10, 20, 50, and 100. Samples only with one revolution ($n = 1$) can be seen as

green bodies, since most matrix materials are known to need at least a partial turn for compaction. The samples with $n = 100$ were subjected to intense friction heating, which could influence the ceramic phase fractions. Furthermore, different BTO particles sizes (BTO-a and BTO-b) were tested, as larger particle sizes could prevent a premature size effect.

For MMCs with ZrO_2, additionally a lower pressure of 6.7 GPa was also used, which had an influence on the phase fraction as discussed later.

To analyze crack propagation behavior, also larger HPT samples with a diameter of about 20 mm were synthesized (HPT Typ-H2-440-1 002 008 Nr.01813). The applied pressure was 8.2 GPa for pure Cu and Cu + ZrO_2 samples. Additional samples produced from bulk Cu pieces, in contrast to the powders, were pressed at 5.7 GPa.

5. Microstructural and Thermal-Analysis

To characterize the microstructure, at first, optical microscope images were taken and compared. As expected, the difference in the visible microstructure is seen along the radial axis (see **Figure 4**): the further away from the center, the smaller the ceramic agglomeration. This is due to ε_{eq}, which is proportional to the radius (see Equation (1)). This also relates to the hardness along the axis. For example, as seen in **Table 5**, the hardness along the diagonal sinks toward the center. This is a common phenomenon, since the microstructure has a larger grain size in the center.

TKD was performed because the grain size especially near the edges of the specimens are too small for standard EBSD (see **Figure 5**). From the microstructural analysis, it can be concluded that the average grain size for pure copper is 32 nm, while the mixture with ceramic particles results in 138 nm.

Tests on structural and thermal stability showed that the ceramic particles have no negative influence on the final material performance (see **Figure 6**); with regard to the mechanical contrasts between ceramic and metal, in particular. The mechanical heterogeneity causes a complex stress strain state in the vicinity of the ceramic to metal interface.[50] This statement is supported
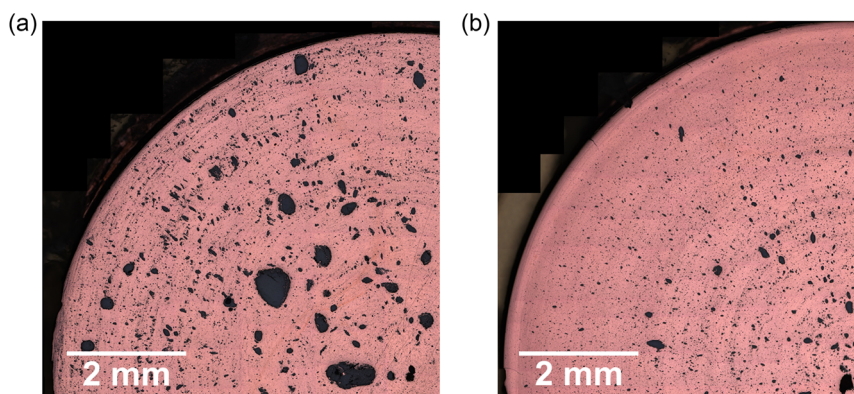
Table 4. Sample variations for MMCs with BTO-a (2 µm), BTO-b (45 µm), and ZrO_2 particles used for XRD measurements with pressure (*GPa*) and rotation number n.

Ceramic	Pressure [GPa]	n					
BTO-a	7.7	1	5	10	20	50	100
	4.6	1	5	10	20	50	100
	2.5	1	5	10	20	50	
BTO-b	7.7	1	5	10	20	50	100
	4.6	1	5	10	20	50	100
	2.5	1	5	10	20	50	100
ZrO_2	7.7	1	5	10	20	50	100
	6.7	1	5	10	20	50	

Figure 4. a) Cu BTO with $n = 5$ and b) Cu BTO with $n = 20$ by optical microscopy.

Table 5. Hardness along a cross section of a large Cu ZrO$_2$ sample with the diameter of 20 mm and applied pressure of 8.2 GPa.

Distance [mm]	−15	−10	−5	Center	+5	+10	+15
HV 0.2	286	281	272	244	247.5	281.4	280
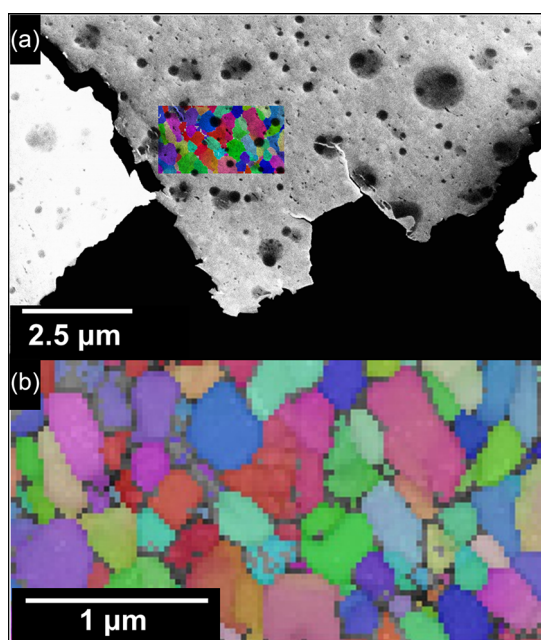
Figure 5. Cu ZrO$_2$: a) scanning electron microscope (SEM) image and b) electron backscatter diffraction (EBSD) inverse pole figure-Z colored image.

Figure 6. Heating curve with the corresponding Vickers hardness HV 0.05 and standard deviation for pure Cu, Cu with BTO, and Cu with ZrO$_2$.

fracture or to interfacial failure.[50] This is especially the case between Cu and ZrO$_2$ with a high difference in elastic modulus, there the stress induced by the matrix leads to particle fracturing and therefore a well-dispersed particles in the matrix. However, between Cu and BTO, the difference is rather small and smaller particles might cluster and form agglomerates. This was fortunately not the case. Based on EDX maps the particles were finely distributed in the matrix. The mechanical contrast also has an effect on the ceramic phases, since an residual internal stress state is present. A plastically deformed matrix that has a higher elastic modulus can exert compression on the ceramic particles. This is the case for Cu and BTO, but not for ZrO$_2$, whereby a tensile state can be expected. If the residual stress state stabilizes a certain phase, very shortly after the pressure between the HPT anvils is removed, destabilizing aging is expected to start.

6. Functionalization of MMCs with BTO

6.1. XRD Analysis

The XRD analysis revealed the presence of a high-pressure phase for samples made from both the BTO-a (smaller mesh size) and the BTO-b (larger mesh size) powder. The tetragonal BTO phase matched with ICDD PDF card # 00-071-0482 and the cubic BTO phase with the card # 04-002-7282. Caused by the

by finite-element simulations.[51] Ceramic reinforcements not only have a higher yield stress, but can also trigger premature internal damage.[52] With regard to geometry, a high angularity of the particles, even for slight roughness or imperfections, increases the local stress concentration at edges. This not only leads to accelerated plastic damage accumulation and pore formation in the matrix nearby the interface, but also to particle

aforementioned stretch of the unit cell a peak split of $<1°$ occurred for almost every cubic peak. The most pronounced peaks of interest for the phase transition are the ones between $30°$ and $33°$.

Due to the proximity of the 110 cubic peak with the 101 and 110 tetragonal peaks, they appear superimposed and overlapping. As a result, when one of the phase fractions increases, the associated peaks also change in shape significantly. The peaks' shoulders can be more pronounced due to an existing tetragonal component. In a qualitative analysis, cubic BTO could therefore be overseen if the observer is not careful enough.

Fitting peaks of tetragonal BTO were comparatively broader than cubic BTO peaks, which fits well to the core–shell model, where the cubic BTO core equates to a larger grain size. The smaller tetragonal BTO peak and the cubic BTO peak shift to lower angle, which indicates an enlargement of the lattice parameters.

Due to grain refinement through HPT, the enclosing peaks were broadened. In the associated BTO sample series, FWHM increases proportionally with increasing number of HPT revolutions. A peak shift was not detected.

Concerning BTO-a, the stabilization of the metastable phase seems to be independent of the applied pressure, as long as it is within the stable pressure range (see **Figure 7**a). The amount of high-pressure phase is about 40% and assuming that it is only caused by the compression of the matrix, then any additional percentage would have to be due to an additional size effect of the ceramics. The high-temperature comparison sample produced at $300°C$ with $n = 50$ had only about 30% of cubic phase, which can also be explained by compression, as the Cu matrix experiencing $300°C$ is not able to apply the same amount of compression stress to the ceramic.

For BTO-b samples, the picture is different. There is a stronger pressure influence on the amount of cubic BTO (Figure 7b). It can be assumed that the particle size difference between BTO-a and BTO-b will cancel out, due to refinement during HPT, and lead to a similar saturation at some point, regardless of applied pressure. This is visible in the results for BTO-b samples processed at pressures of 4.6 and 2.5 GPa, at $n > 5$.
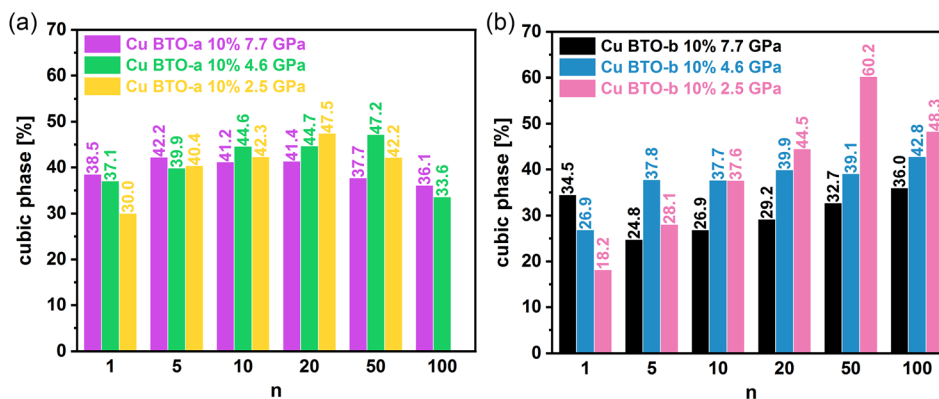

Figure 8. c/a ratio for different BTO samples with the related n.

From **Figure 8**, the c/a ratio can be seen. The ratio increases to greater asymmetry of the unit cell with increasing number of revolutions (n). This is apparently an effect of the consolidation during the HPT process, which can lead to large shearing of the particles. The high-temperature reference sample turned at $300°C$ had the highest symmetry at about $c/a = 1.01$, similar to the BTO-b 2.5 GPa, $n = 1$ sample. Based on the results, the c/a ratio only indicates that the existing asymmetric fraction becomes even more asymmetric with increasing n.

6.2. Aging and Matrix Relaxation

To check if the BTO phase is stable over a long time, a dedicated sample was measured directly after synthesis and after 2 months of storage at ambient conditions (see **Figure 9**). The phase fraction of c-BTO decreased by about 10%. This reduction could be the result of stress relaxation of the Cu matrix, which also reduces the compressive stress imposed onto the BTO particles. This is a clear hint that c-BTO is at least partially stabilized by residual stresses.

Figure 7. Comparison of the cubic phase fraction in a) Cu BTO-a samples and b) Cu BTO-b samples, for the different anvil pressures and number of rotations n.
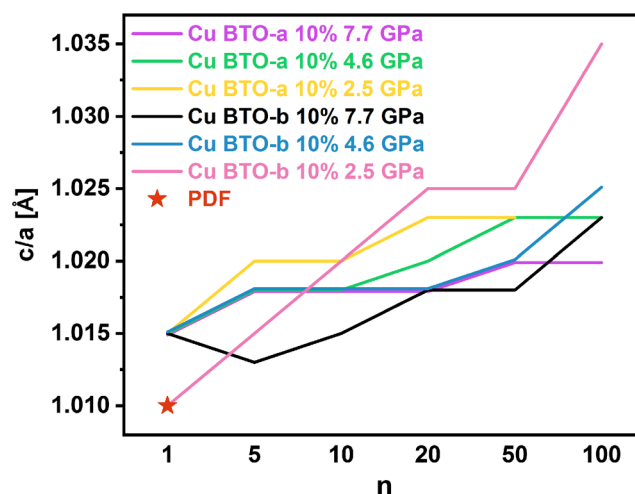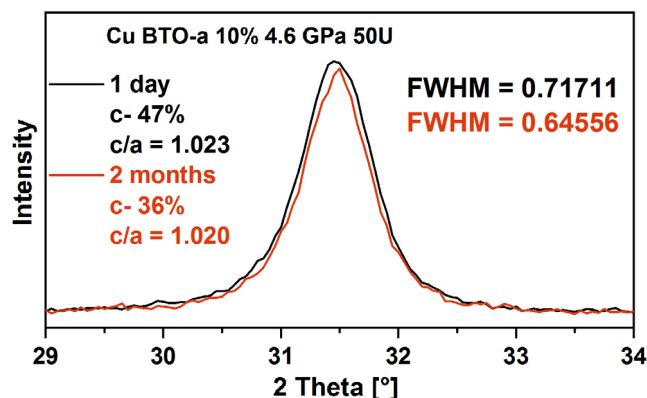
ADVANCED
SCIENCE NEWS

www.advancedsciencenews.com

ADVANCED
ENGINEERING
MATERIALS

www.aem-journal.com

Figure 9. X-ray diffraction (XRD) scans of a sample with 10% BTO-a, processed at 4.6 GPa, $n = 50$, aged 1 day and 2 months.

Figure 11. Potential difference across a BTO particle indicated by arrows in Figure 10c,d.

6.3. Piezoelectric Stimulation by SKPFM

Similar to recent work by He et al.[53] conducted on monocrystalline BTO, the contact potential difference (V_{CPD}) for cubic BTO and tetragonal BTO is around 200 mm, meaning that the presence of tetragonal BTO can be detected by SKPFM.

Figure 10a,b shows the topography of the sample before and after *in situ* bending, indicating that indeed the same area had been mapped. The white scattered specks are most likely residues of the polishing suspension, which could not be cleaned away completely due to the fragility of the drilled samples. Figure 10c,d shows the associated contact potential maps. The
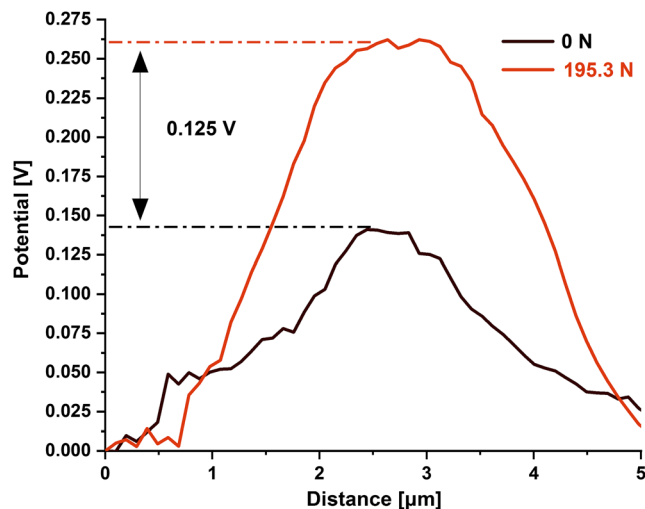
light areas emerge after deformation, exhibiting a different surface energy, which is the result of the activated piezoelectric effect created by the mechanical deformation of the BTO particles.

A scan across a prominent BTO particle in the center of Figure 10 (direction and position indicated by arrows) is presented in **Figure 11**. About 40% of BTO is cubic in advance of the measurement. Since the probe tip samples a signal from an extended interaction zone, the largest signal is located in the
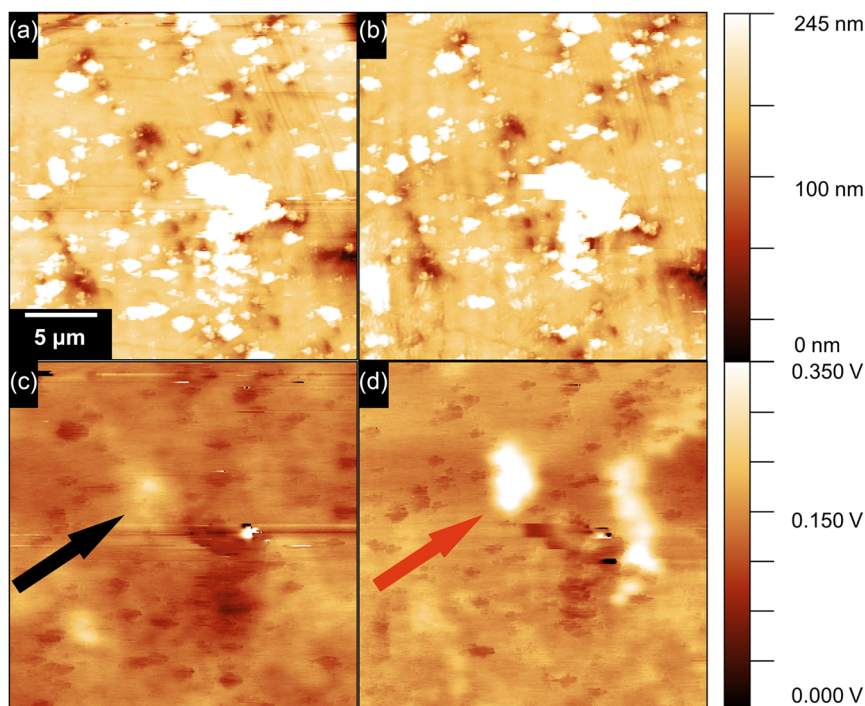

Figure 10. Scanning Kelvin probe force microscopy (SKPFM) measurement of a sample with 10 wt% BTO, processed at 2.5 GPa, $n = 5$, with 40% cubic BTO (determined by XRD analysis): a,b) topography and c,d) potential maps in the state a,c) before bending and b,d) after bending with an applied force of 195.3 N.

center of a BTO cluster or particle. The deformed specimen also shows a plateau, which reflects exactly this assumption. The maximal measured potential difference between Cu and the BTO particle was 260 mm, while the difference between the peaks in the middle of the particle is 125 mm. This is not in line with the measured contact potential difference published by He et al.[53] (200 mm). Indeed, it is not unusual that absolute values from SKPFM differ because the results are very sensitive to the surface state of the measured material and the tip itself.[54] If 260 mm represents the tetragonal BTO level, then 50 mm should represent cubic BTO. At the start of the line scan in Figure 11, a hint of a plateau around 50 mm can be seen, indicating a V_{CPD} of 210 mm between cubic BTO and tetragonal BTO. Nonetheless, the different measured potentials before and after loading are sufficient to prove functionalization.

7. Functionalization of MMCs with Zirconia

7.1. XRD Analysis

The XRD analysis revealed the presence of a high-pressure phase for ZrO_2. For ZrO_2 samples, the analysis was straightforward, since with the appearance of t-ZrO_2, a prominent tetragonal peak 101 rises between the monoclinic peaks $\bar{1}11$ and 111. Monoclinic ZrO_2 matched with ICDD PDF card # 04-015-4188 and t-ZrO_2 with card # 04-016-1792.

As supported by the particle size distribution results (Table 1), some of the ZrO_2 particles were already at such small sizes before HPT processing, that the powder already transformed to t-ZrO_2 due to the size effect. Further XRD analysis of the ZrO_2 raw powder confirmed that 6.5% of the powder were already tetragonal at this stage. All further presented percentages for ZrO_2 phase fraction were therefore subtracted by that amount. Similar to Edalati et al., the more pronounced $\bar{1}11$ peak intensity shifted toward the 111 peak. This seems to be a preferential orientation effect of the HPT.[10] The 101 peak of the tetragonal phase would also have fit well with the position of the 121 orthorhombic peak. However, considering other peaks of the orthorhombic phase, for example, 002 and 020, the presence of this phase could be excluded.[55] In the same way, also the presence of the cubic phase could be excluded. However, this does not eliminate the possibility that these other phases were actually formed during HPT. The absence of the phases only means that they could not be stabilized. In addition to the 111 peak, also the 200 and the 110 were more pronounced after HPT. Most likely is this due to the texture changes of the Cu matrix since the 111 orientation matches the most significant slip system for Cu the deformation process, as defined by the stress and constraint between grains.[56] Interestingly, this matches also the 111 texture of ZrO_2 and is likely related to the matrix texture, but could also be independently induced by the HPT processing route. Furthermore, the Cu matrix shows anisotropic peak broadening for the 200 peak, which could be caused by stacking faults, other crystallographic faults, and strain.

Regarding **Figure 12**, the pronounced {111} monoclinic ZrO_2 peaks are visible for $n = 1$ to $n = 5$. With further increasing revolutions, the 101 t-ZrO_2 peak intensity increases, indicating the increasing tetragonal phase fraction, and seems to shift toward a
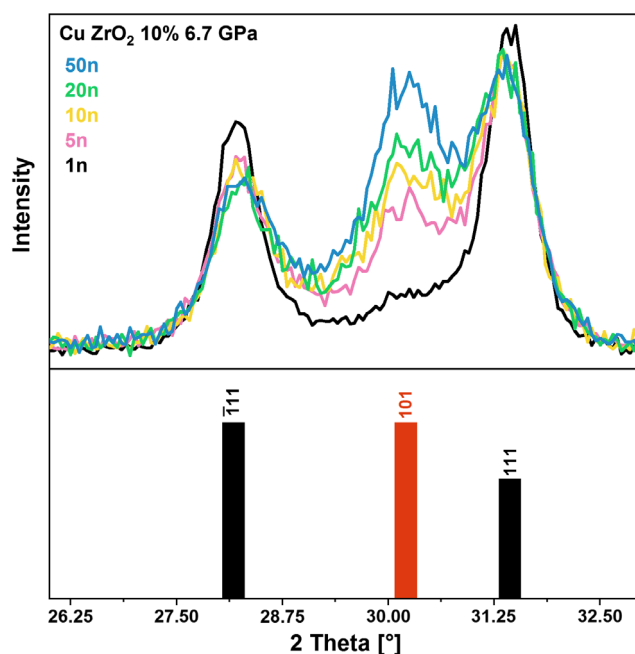

Figure 12. XRD patterns of Cu ZrO_2 samples, indicating monoclinic and tetragonal peaks in black and red, respectively.
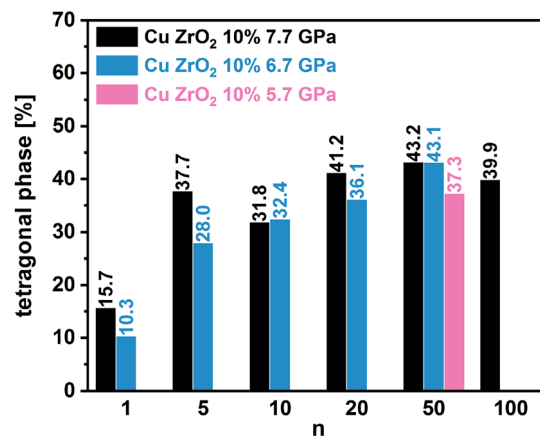

Figure 13. Comparison of the evaluated phase fraction at different pressures and n for tetragonal ZrO_2.

smaller angle (about 0.1°). This, in addition to the stress-induced shift caused by the HPT, could be due to a changing crystal structure.[10]

The same observation was made for the tetragonal ZrO_2 peaks 103 and 211 in the higher-angle region (not presented here). The less pressure was applied, the more gradual was also the transition toward tetragonal ZrO_2 (see **Figure 13**). At the highest tested pressure, the metastable phase fraction was seen to saturate at ≈40%. Theoretically, pressure should have an opposing effect on the desired phase transition. Therefore, similar to BTO, the proportional correlation between n and tetragonal ZrO_2 phase fraction can be attributed to the size effect, especially because the expected microstructure saturation for the Cu matrix has a similar dependence on n.[56]

**ADVANCED
SCIENCE NEWS**

www.advancedsciencenews.com

**ADVANCED
ENGINEERING
MATERIALS**

www.aem-journal.com

Since the sample size of ZrO_2 for crack propagation testing (large HPT samples) had to be increased, the scalability could be an issue. A comparison between the tetragonal phase fraction for both a small and large disk processed at 5.6 GPa for 50 turns showed rather similar values of 37% and 40%, respectively, thereby making the assumed scalability plausible.

For the large HPT samples, a pressure of 8.6 GPa was also tested and interestingly resulted in a decreased tetragonal fraction of only 23%. It seems that pressures exceeding 7.7 GPa are not able to produce the desired high amount of tetragonal phase. The thermal load in both pressure ranges should be similar, therefore the microstructural recovery of the Cu should not affect the tetragonal phase fraction significantly. A more likely reason for the observed decrease is the probably the transformation of tetragonal ZrO_2 to a further cubic phase above 8 GPa, which apparently presents an additional upper pressure limit for the stabilization of the desired phase.

7.2. Crack Initiation Retardation and Crack Closure

To investigate if ZrO_2 provides a retardation of crack initiation, a cyclic R-curve determination was conducted according to Maierhofer et al.[44] This procedure allows for the determination of the intrinsic threshold for fatigue crack growth $\Delta K_{th,eff}$, the ΔK_{th} value under absence of plasticity-induced crack closure. Therefore, an increase in $\Delta K_{th,eff}$ is a clear sign for an additional crack closure mechanism, originating from an increase in volume from a martensitic phase transformation by tensile stresses in the process zone of the fatigue crack.

Using the cyclic R-curve technique, the onset of fatigue crack growth $\Delta K_{th,eff}$ can be determined, especially if the crack is
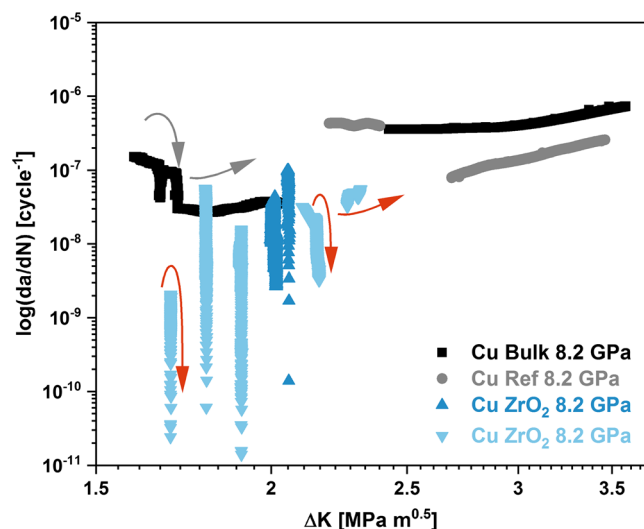
Figure 15. Crack length a from DPCP method against N for the 8.2 GPa Cu ZrO_2 sample. Below $\Delta K = 1.9\,MPa\sqrt{m}$ cracks are not able to grow, whereas above $\Delta K = 1.9\,MPa\sqrt{m}$ and up to $\Delta K = 2.1\,MPa\sqrt{m}$ cracks start to grow but decelerate with advancing crack length. Above $\Delta K = 2.1\,MPa\sqrt{m}$ cracks are initiated finally and grow to final failure.

Figure 14. Crack growth curves for short cracks in the reference specimens (grey, black) and ZrO_2–MMC specimens (blue) with arrows showing the direction of advancing load cycles. Especially for the blue curves from the MMCs, the deceleration, although partially after prior crack re-initiation, until $\Delta K = 2.1\,MPa\sqrt{m}$, is obvious. The cracks in the reference material start crack growth to final failure and thus without a later deceleration already a $\Delta K = 1.7\,MPa\sqrt{m}$.
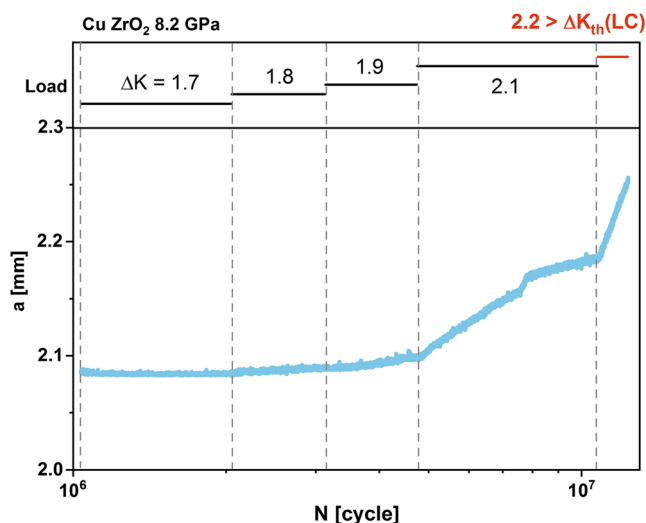
arrested again by the evolving crack closure mechanisms during a further crack growth by ongoing fatigue. These closure mechanisms lead then to crack deceleration and arrest. If the crack no longer stops advancing, ΔK_{th} is exceeded and a crack grows to final failure.

The reference Cu samples already showed signs of advancing crack growth at $\Delta K = 1.6\,MPa\sqrt{m}$ with an again arrested crack (see **Figure 14**). ΔK_{th} is finally exceeded at $K = 1.9\,MPa\sqrt{m}$.

Hence, the question arises whether the specimens, which were made from a high-purity solid Cu rods (bulk samples) and not from a powder like the other specimens, can be compared with each other. The difference between the two determined thresholds would indicate, that they are not very similar and apparently the powder route leads to a better stability. Even if these two samples would differ greatly, the subsequent measurement data (see Figure 14, black and gray curves) indicated comparable fatigue crack growth behavior. So, the bulk sample is taken as a reference.

For samples with ZrO_2 (**Figure 15**), this value increased to the threshold of $2.1\,MPa\sqrt{m}$. Therefore compared to the reference bulk sample, the addition of ZrO_2 developed the predicted closure mechanism through volume expansion. As seen in Figure 14, the crack propagation rate is increased for the samples without ZrO_2 and are visibly growing underneath the threshold of $2.2\,MPa\sqrt{m}$. This is a good indication for the desired additional crack closure mechanism.

K_{IC} values, measured in accordance to ASTM E399, of $9.4\,MPa\sqrt{m}$ for samples with ZrO_2 and of $7.1\,MPa\sqrt{m}$ for samples without ZrO_2 are in line with the literature values, though for a composite material with ZrO_2 on the higher end.[57] This also indicated that the addition of the zirconia not only prolongs the fatigue lifetime of the material but also increases the fracture toughness.

**ADVANCED
SCIENCE NEWS**

www.advancedsciencenews.com

**ADVANCED
ENGINEERING
MATERIALS**

www.aem-journal.com

8. Conclusion

The aim of this work was to create functionalized MMCs. For this purpose, two strategies were selected: a sensory activation under stress with the aid of BTO and a crack retardation ability with the aid of ZrO_2. Each was implemented via HPT using a Cu model matrix. Suitable pressure ranges were selected, and their limits for stabilization of the respective high-pressure ceramic phases were explored. Particle distributions and relevant functional properties were investigated. The functionalization of the produced samples was successfully validated. For BTO, the expected change in electrical polarization could be measured using SKPFM and for ZrO_2, additional crack closure could be measured in terms of cyclic R-curves. Accordingly, the objective of the work was confirmed satisfactorily and in the scope of the question two *smart* MMCs have been created.

Some improvements could be made in the future: 1) The temperature can be controlled during synthesis to enable targeted microstructure adjustment. 2) The selected matrix material should be exchanged for a more thermally and mechanically stable one. This exchange could lead to improved percentage of the stabilized high-pressure phase. 3) Microstructural saturation correlates to the amount of phase stabilization, therefore more data for lower revolution rates could elucidate information on the evolution of phase composition. 4) The combination of BTO and ZrO_2 could provide an MMC with improved fatigue performance and damage-sensing ability.

Conflict of Interest

The authors declare no conflict of interest.

Data Availability Statement

The data that support the findings of this study are available from the corresponding author upon reasonable request.

[1] K. Edalati, *Adv. Eng. Mater.* **2019**, *21*, 1800272.

[2] A. Dorri Moghadam, B. F. Schultz, J. B. Ferguson, E. Omrani, P. K. Rohatgi, N. Gupta, *JOM* **2014**, *66*, 872.

[3] M. Yadollahpour, S. Ziaei-Rad, F. Karimzadeh, J. Eskandari-Jam, *Simul. Modell. Pract. Theory* **2011**, *19*, 337.

[4] A. Etaati, A. Shokuhfar, E. Omrani, P. Movahed, H. Bolvardi, H. Tavakoli, In , Vol *297*, Trans Tech Publications, Switzerland **2010** pp. 489–494.

[5] E. Omrani, A. Shokuhfar, A. Etaati, A. Dorri, M. A. Saatian, in , Vol *297*, Trans Tech Publications, Switzerland **2010** pp. 344–350.

[6] M. A. Taha, M. Zawrah, *Ceram. Int.* **2017**, *43*, 12698.

[7] P. K. Rohatgi, D. M. Afsaneh, B. F. Schultz, J. B. Ferguson, F. Marquis, Wiley, Hoboken, NJ **2013**.

[8] P. W. Bridgman, *Phys. Rev.* **1935**, *48*, 825.

[9] Y. Cao, S. Ni, X. Liao, M. Song, Y. Zhu, *Mater. Sci. Eng.: R: Rep.* **2018**, *133* 1.

[10] K. Edalati, S. Toh, Y. Ikoma, Z. Horita, *Scr. Mater.* **2011**, *65*, 974.

[11] T. Asare, Ph.D. Thesis, Virginia Tech, **2004**.

[12] D. W. Müller, S. Lößlein, E. Terriac, K. Brix, K. Siems, R. Moeller, R. Kautenburger, F. Mücklich, *Adv. Mater. Interfaces* **2021**, *8*, 2001656.

[13] C. Das, A. Shahee, N. Lalla, T. Shripathi, *Proc. of the 54th DAE Solid State Physics Symp.*, **2009**, pp. 439–440.

[14] B. Jiang, J. Iocozzia, L. Zhao, H. Zhang, Y.-W. Harn, Y. Chen, Z. Lin, *Chem. Soc. Rev.* **2019**, *48*, 1194.

[15] D. Y. He, X. R. Xing, L. J. Qiao, A. A. Volinsky, *Appl. Surf. Sci.* **2014**, *311* 837.

[16] M. Lambert, R. Comes, *Solid State Commun.* **1969**, *7*, 305.

[17] L. Feng-Ying, J. Chang-Qing, Y. Shu-Jie, X. Chang-Jiang, Y. Ri-Cheng, W. Xiao-Hui, L. Jing, L. Xiao-Dong, L. Yan-Chun, C. Liang-Chen, *Chin. Phys. Lett.* **2006**, *23*, 1249.

[18] B. Ravel, E. A. Stern, R. I. Vedrinskii, V. Kraizman, *Ferroelectrics* **1998**, *206*, 407.

[19] T. Ishidate, S. Abe, H. Takahashi, N. Môri, *Phys. Rev. Lett.* **1997**, *78*, 2397.

[20] J. Íniguez, D. Vanderbilt, *Phys. Rev. Lett.* **2002**, *89*, 115503.

[21] J. E. Spanier, A. M. Kolpak, J. J. Urban, I. Grinberg, L. Ouyang, W. S. Yun, A. M. Rappe, H. Park, *Nano Lett.* **2006**, *6*, 735.

[22] G. A. Samara, *Phys. Rev.* **1966**, *151*, 378.

[23] Y. Huan, X. Wang, J. Fang, L. Li, *J. Eur. Ceram. Soc.* **2014**, *34*, 1445.

[24] K. Uchino, E. Sadanaga, T. Hirose, *J. Am. Ceram. Soc.* **1989**, *72*, 1555.

[25] A. Frenkel, M. Frey, D. Payne, *J. Synchrotron Radiat.* **1999**, *6*, 515.

[26] A. F. Devonshire, *Lond. Edinbur. Dublin Philos. Mag. J. Sci.* **1949**, *40*, 1040.

[27] T. Lee, I. A. Aksay, *Cryst. Growth Des.* **2001**, *1*, 401.

[28] T. Hoshina, S. Wada, Y. Kuroiwa, T. Tsurumi, *Appl. Phys. Lett.* **2008**, *93*, 192914.

[29] T. Hoshina, *J. Ceram. Soc. Jpn.* **2013**, *121*, 156.

[30] U. D. Venkateswaran, V. M. Naik, R. Naik, *Phys. Rev. B* **1998**, *58*, 14256.

[31] S. Aoyagi, Y. Kuroiwa, A. Sawada, I. Yamashita, T. Atake, *J. Phys. Soc. Jpn.* **2002**, *71*, 1218.

[32] Y. Akishige, J. Nakahara, E. Sawaguchi, *J. Phys. Soc. Jpn.* **1991**, *60*, 1115.

[33] G. K. Bansal, A. H. Heuer, *Acta Metallurgica* **1972**, *20*, 1281.

[34] A. H. Heuer, N. Claussen, W. M. Kriven, M. Ruhle, *J. Am. Ceram. Soc.* **1982**, *65*, 642.

[35] A. Fathy, A. Wagih, A. Abu-Oqail, *Ceram. Int.* **2019**, *45*, 2319.

[36] P. Jha, P. Gupta, D. Kumar, O. Parkash, *J. Compos. Mater.* **2014**, *48*, 2107.

[37] A. H. De Aza, J. Chevalier, G. Fantozzi, M. Schehl, R. Torrecillas, *Biomaterials* **2002**, *23*, 937.

[38] A. G. Evans, A. H. Heuer, *J. Am. Ceram. Soc.* **1980**, *63*, 241.

[39] J. F. Shackelford, R. H. Doremus, *Ceramic And Glass Materials*, Springer, New York **2008**.

[40] R. Garvie, *J. Phys. Chem.* **1978**, *82*, 218.

[41] A. Abu-Oqail, A. Wagih, A. Fathy, O. Elkady, A. M. Kabeel, *Ceram. Int.* **2019**, *45*, 5866.

[42] W. A. Dollase, *J. Appl. Crystallogr.* **1986**, *19*, 267.

[43] G. Caglioti, A. T. Paoletti, F. P. Ricci, *Nucl. Instrum.* **1958**, *3*, 223.

[44] J. Maierhofer, S. Kolitsch, R. Pippan, H.-P. Gänser, M. Madia, U. Zerbst, *Eng. Fract. Mech.* **2018**, *198*, 45.

[45] U. Zerbst, M. Vormwald, R. Pippan, H.-P. Gänser, C. Sarrazin-Baudoux, M. Madia, *Eng. Fract. Mech.* **2016**, *153*, 190.

[46] H. H. Johnson, *Mater. Res. Stand.* **1965**, *5*, 442.

[47] H. H. Johnson, P. C. Paris, *Eng. Fract. Mech.* **1968**, *1*, 3.

[48] T. Hebesberger, H.-P. Stüwe, A. Vorhauer, F. Wetscher, R. Pippan, *Acta Mater.* **2005**, *53*, 393.

[49] A. P. Zhilyaev, T. G. Langdon, *Progr. Mater. Sci.* **2008**, *53*, 893.

[50] V. A. Romanova, R. R. Balokhonov, S. Schmauder, *Acta Mater.* **2009**, *57*, 97.

[51] S. Qin, C. Chen, G. Zhang, W. Wang, Z. Wang, *Mater. Sci. Eng.: A* **1999**, *272*, 363.

[52] A. Mortensen, J. Llorca, *Annu. Rev. Mater. Res.* **2010**, *40* 243.

[53] D. He, X. Tang, Y. Liu, J. Liu, W. Du, P. He, H. Wang, *Materials* **2021**, *14*, 4463.

[54] P. Gruenewald, N. Hautz, C. Motz, *Int. J. Hydrogen Energy* **2022**, *47*, 15922.

[55] O. Ohtaka, H. Fukui, T. Kunisada, T. Fujisawa, K. Funakoshi, W. Utsumi, T. Irifune, K. Kuroda, T. Kikegawa, *Phys. Rev. B* **2001**, *63*, 174108.

[56] H. Jiang, Y. T. Zhu, D. P. Butt, I. V. Alexandrov, T. C. Lowe, *Mater. Sci. Eng.: A* **2000**, *290*, 128.

[57] T. K. Gupta, F. F. Lange, J. H. Bechtold, *J. Mater. Sci.* **1978**, *13*, 1464.

[58] A. S. Verma, A. Kumar, *J. Alloys Compd.* **2012**, *541* 210.

[59] J. K. Dewhurst, J. E. Lowther, *Phys. Rev. B* **1998**, *57*, 741.

[60] M. Fischer, A. Polian, *Phase Transit. A Multinat. J.* **1987**, *9*, 205.